*Journal of Marine Systems*, 3 (1992) 321–342
Elsevier Science Publishers B.V., Amsterdam



# A model study of "bump" induced western boundary current variabilities

Lie-Yauw Oey [a,b], Tal Ezer [b], George L. Mellor [b] and Ping Chen [a]

[a] *Department of Civil and Ocean Engineering, Stevens Institute of Technology, Hoboken, NJ 07030, USA*
[b] *Program in Atmospheric and Oceanic Sciences, Sayre Hall, Forrestal Campus, Princeton University, Princeton, NJ 05844, USA*

(Received September 10, 1991; revised version accepted December 20, 1991)

ABSTRACT

Oey, L.-Y., Ezer, T., Mellor, G.L. and Chen, P., 1992. A model of "bump" induced western boundary current variabilities. J. Mar. Syst., 3: 321–342.

A time-dependent, three-dimensional numerical model is used to study the effects of a bottom irregularity or "bump" on western boundary current (WBC) variabilities along a simplified shelf and slope. Numerical experiments with (i) no bottom bump, (ii) a small bump and (iii) a large bump have been conducted. Case (i) produces low variabilities and cases (ii) and (iii) show significant increase in slope and shelf energetics both downstream and upstream of the bump. Disturbances generated at the bump are well correlated with flow variabilities upstream. Downstream variabilities are caused by meander development following the WBC deflection by the bump, while topographic waves excite upstream variabilities. The model also indicates two modes of deflection paths, small- and large-amplitude paths, downstream of the bump. These findings are further supported by results obtained from a Gulf Stream simulation which incorporates the bathymetry of the U.S. South Atlantic Bight, and which has a more realistic boundary forcing. The simulated eddy kinetic energy distribution shows three regions of variability which are of interest: one inshore (and slightly downstream) and one offshore of the Charleston Bump, and a third region over the shelfbreak some 150–200 km upstream of the Bump. The inshore and offshore maxima are due to the small and large amplitude deflection paths of the model Gulf Stream, respectively, while the upstream maximum is presumably due to topographic wave activity.

## Introduction

Frontal meanders often develop along a western boundary current (WBC) on a continental shelfbreak/slope. These meanders have been documented extensively for the Gulf Stream (GS) in the U.S. southeastern continental shelf and slope (the South Atlantic Bight or SAB), where they are found to have cross-stream and along-stream length scales of approximately 30–80 km and 150–250 km, respectively (see, e.g., Lee and Atkinson, 1983; Bane, 1983). Here, the northward-flowing GS encounters a topographic feature, the "Charleston Bump" (henceforth the "Bump") over the continental slope at 31.5 to 32°N. Meanders are often formed downstream of the Bump (Bane, 1983). On the other hand, frontal meanders are also observed upstream of the Bump (Lee and Atkinson, 1983). Because of the proximity of these meanders to the shelf, their effects on the circulation, mixing and ecology of the shelf are important.

Previous numerical model studies have shown that dynamical (in particular, baroclinic) instability is important to the development of meanders (Orlanski and Cox, 1973; Chao and Kao, 1978; James, 1987; Oey, 1988; Wood, 1988). Models produce realistic-looking meanders for a constant-depth topography. However, the meanders

*Correspondence to:* Dr. L.-Y. Oey, Program in Atmospheric and Oceanic Sciences, Sayre Hall, Forrestal Campus, Princeton University, Princeton, NJ 05844, USA.

are of smaller amplitudes when bottom slope is introduced (Orlanski and Cox, 1973), unless the Stream's frontal position is explicitly perturbed (Xue, 1991). For a WBC deflected by a bottom bump, large-amplitude meanders can be expected, perhaps as a result of resonant interaction of the forced response with the baroclinic instability of the current (Mitsudera and Grimshaw, 1991). In a model study of a WBC deflected by a coastal wall, Oey and Chen (1991, henceforth OC) found enhanced current variability at locations which coincide approximately with multiples of the topographic standing-wave length upstream of the wall. Thus it is possible for energetic meanders to develop upstream as well as downstream of the bump. In the presence of a bump, then, modeled meander amplitudes can be in better agreement with observations even with the stabilizing effect of a continental slope.

Observations on the continental rise northeast of Cape Hatteras support the idea that topographic waves can exist upstream of a meander-generation region of the WBC. There is evidence that west-southwestward propagating topographic waves are generated by Gulf Stream meanders in the vicinity of the New England seamount chain (Thompson, 1977; Hogg, 1981; Csanady, 1986). In the SAB, one expects that topographic waves are also generated upstream of the Charleston Bump, by meanders produced near the Bump. This paper presents numerical experiments in an effort to understand WBC meander development due to a Bump, and its consequences on the shelf and slope current variability. In particular, we wish to study velocity and temperature fluctuations produced upstream of the bump. The next section presents the idealized model and the third section the results obtained with and without bumps. In the fourth, the results obtained from a model simulation with SAB bathymetry and realistic forcing are presented. The paper ends with a concluding discussion.

## The model

The model (Blumberg and Mellor, 1983; Oey et al., 1985) solves equations for the three-dimensional velocity $\boldsymbol{u}$ and temperature $T$, (hence density, with salinity fixed at 35 ppt), and uses the 2.5-level Mellor-Yamada (1982) turbulence closure scheme to parameterize the vertical mixing. Details can be found in the above references and in OC; the following describes only the domain and forcing used in the present application. The model domain (Fig. 1) is 2200 km west to east (the $x$-direction) and 1700 km south to north (the $y$-direction), and is on a $\beta$-plane centered at 31°N. It consists of a semi-enclosed Bight-like

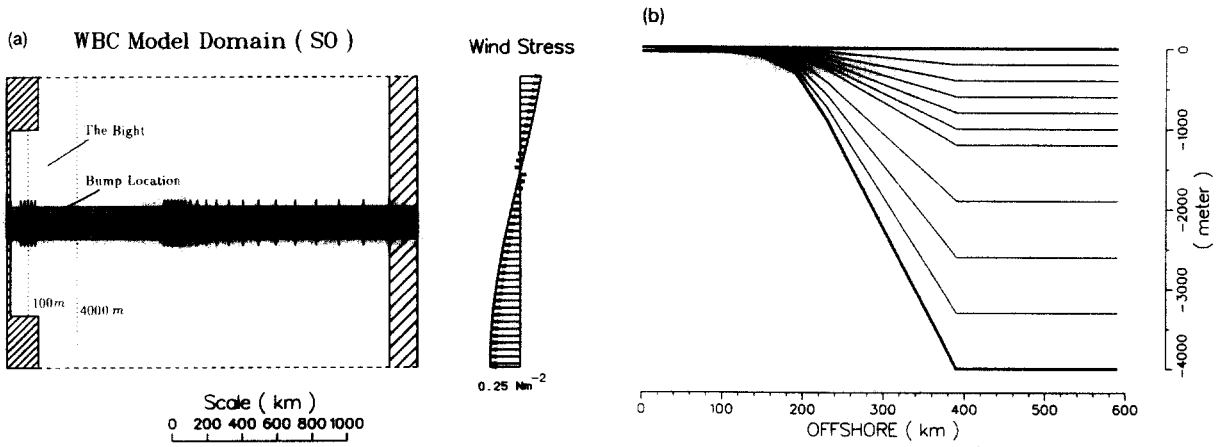


Fig. 1. (a) The model domain used in the experiments SO, SML and SMH. The 100 m isobath on the outershelf, as well as the 4000 m isobath further offshore, are shown as dotted lines. The zonal windstress used is shown on the right-hand panel, where the maximum arrow is 0.25 N m$^{-2}$. The grid distribution used in the main region of interest is also shown. (b) The model's vertical grid distribution across the shelf, slope and the deep ocean.

continental shelf in the mid-latitude of its western portion, in which the depth $H$ is 50 m for the first 100 km from the coast, and increases offshore to 200 m at the shelfbreak. The Bight is approximately 140 km wide, and 1000 km long. The ocean depth increases eastward from 100 m in the outer shelf to 4000 m in the deep ocean, and the depth transition occurs over a continental shelfbreak/slope about 250 km in width. The horizontal grid spacing is variable in $x$, with $\Delta x = 20$ km over the shelf and the western half of the ocean basin, increasing linearly to $\Delta x = 200$ km near the eastern wall; $\Delta y = 20$ km (Fig. 1). The model uses a $\sigma$ coordinate in the vertical, distributed into eleven levels as shown in Fig. 1b. The boundary conditions are as follows. The normal component of momentum and heat fluxes is zero at all horizontal walls. The tangential velocities are set to zero at all horizontal walls except those at the northern and southern boundaries, where free-slip conditions are applied. At the ocean floor, the heat flux is zero while the bottom frictional stress is computed by matching the velocity nearest the bottom ($u_b$) with the logarithmic law of the wall (Oey et al., 1985). As in OC, surface cooling of magnitude 300 W m$^{-2}$ is applied over the shelf to mimic wintertime conditions, and heating is applied over the eastern portion of the main basin ($x > 350$ km) such that the area integrated heat flux is zero. We apply a latitude-dependent zonal windstress as shown on the right hand panel in Fig. 1, to spin up the western boundary current (WBC) or the model "Gulf Stream". To simplify interpretation of flow dynamics in the WBC/shelf, the windstress is applied only over the deep ocean, $x > 350$ km, and therefore serves solely to create a mid-ocean Sverdrup transport and a northward return flow in the western boundary layer along the shelfbreak/slope. A Laplacian horizontal diffusion with coefficient $A$, which is a function of the depth is used such that the WBC is mildly inertial with Reynolds number, $Re = V_a W/A \approx 60$, where $W \approx 50$ km is the half width of the WBC, and $V_a \approx 0.35$ m s$^{-1}$ is the cross-sectional averaged velocity of the WBC just upstream of the Bight's slope. The WBC transport averaged over the final year of a 9 years' calculation is approximately 30 Sv (1 Sv = $10^6$ m$^3$ s$^{-1}$), a fairly realistic value found for the Gulf Stream in the SAB.

The model ocean is initially quiescent and vertically stratified such that $\boldsymbol{u} = 0$ and $T = 10$°C over the shelf where $H < 100$ m, and

$$T = \begin{cases} 25\text{°C} & z > -50 \text{ m} \\ [25 + 22(z + 50)/1450]\text{°C} & \\ & -50\ m > z > +1500 \text{ m} \\ 3\text{°C} & -1500 \text{ m} > z, \end{cases}$$

otherwise; $z$ is the vertical axis, positive upward. Wind and surface heating/cooling are then applied. The calculation continues until it has reached a quasi-steady state with a well-defined WBC along the shelfbreak, and a cooled, well-mixed shelf. The quasi-equilibrium state is reached in about 4 to 5 years, as shown by the kinetic energy time series plots in Fig. 2 (note in particular the plot for the WBC). We have nevertheless carried out the integration through the 8th year. A continued calculation from year 8 through year 9 of this spin-up calculation with a

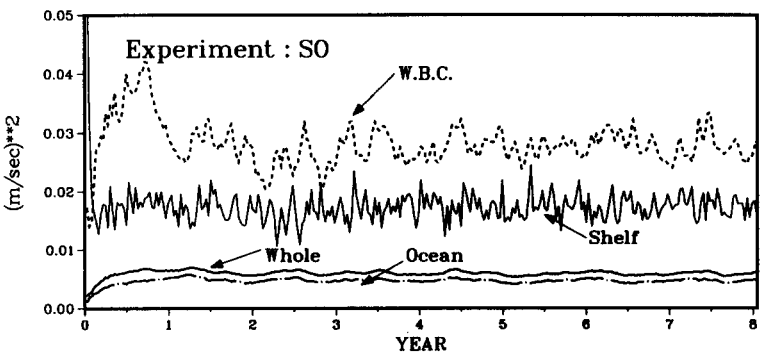


Fig. 2. Experiment SO: kinetic energies averaged over four different regions of the model domain, plotted as a function of time.

$y$-independent shelfbreak/slope isobath (except, of course, for the coastal walls north and south of the Bight) was then carried out and is denoted as experiment S0; this calculation will serve as the control experiment. Two other experiments, SML and SMH, with bumps over the shelfbreak/slope (Fig. 1) have also been conducted. The bumps are of the Gaussian type both with $e$-fold decay scale of 60 km, and are introduced over a period of 10 days starting from year 8 of the spin-up calculation. Both "bump" experiments were integrated for one year each. In experiment SML, the offshore sloping of the bump is "gentle", similar to the Charleston Bump, as shown in Fig. 3a. In experiment SMH, the maximum peak of the bump rises to about 50 m below the free surface (Fig. 3b). In the following, the last 265 days of the results (saved every 1 day) for the three experiments are analyzed, and the means are defined as averages over these last 265 days of the experiments. Thus we allow some 100 days for the flows to settle after the introduction of the bumps in SML and SMH. Experience in OC suggests that this time interval is sufficient. By comparing the results with and without bumps, as well as small and large bumps, we can deduce how perturbations induced at the bump may produce flow variabilities upstream and downstream of the bump.

## Results

In this section we present: (i) the mean temperature and velocity fields; (ii) examples of the time-dependent development of meanders along the model WBC; and (iii) some flow statistics.

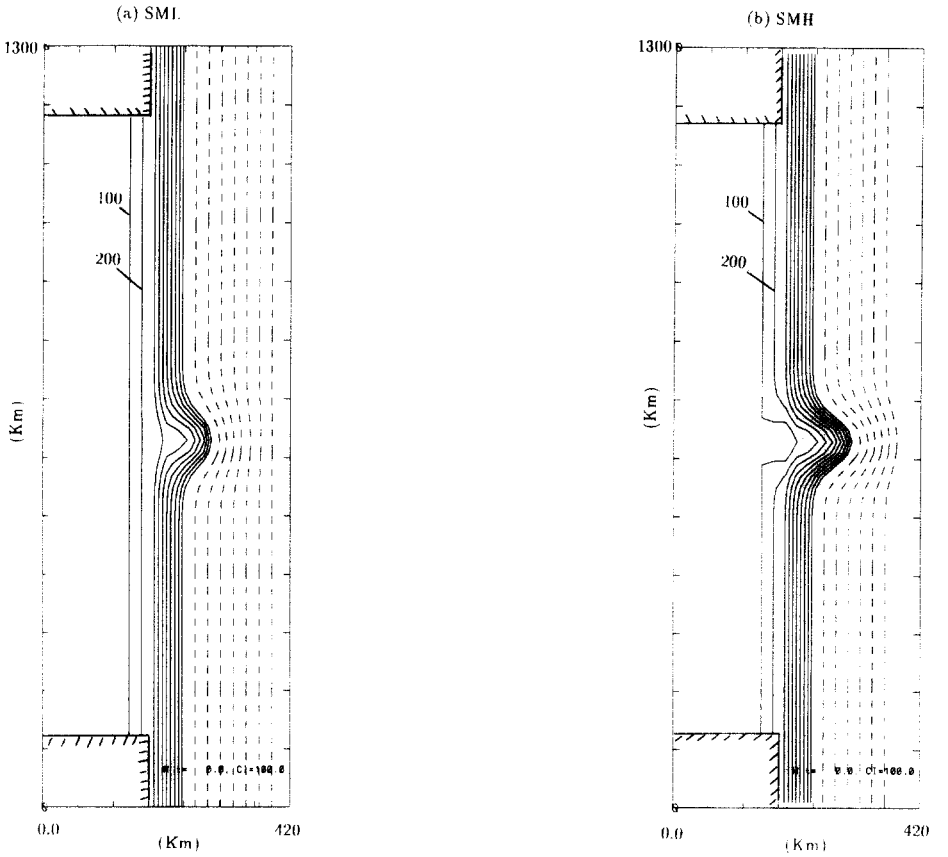


Fig. 3. (a) Bight's bottom topography used for experiment SML. The interval for solid contours is 100 m, and is 400 m for dashed contours. (b) Bight's bottom topography used for experiment SMH. The interval for solid contours is 100 m, and is 400 m for dashed contours.

*The mean fields*

Figure 4 compares the mean near-surface temperature contours, velocity vectors and the vertical velocity contours for experiments SML (a) and SMH (b), plotted in a blown-up region which includes the shelf as well as the WBC in the Bight. This same region will be used for all subsequent plots. For the temperature and horizontal velocities, the first $\sigma$ grid level below the surface is used, while for the vertical velocity, a depth-averaged value over the upper three $\sigma$ levels is used. The vertical velocity is coherent over the depth so that the particular choice of three $\sigma$ grids is not crucial to the results, except that the averaging does smooth out the field a little. The plots for experiment S0 (not included here) shows a WBC parallel to the shelfbreak/slope isobath with small vertical velocity of magnitude everywhere less than $10^{-5}$ m s$^{-1}$. For experiments SML and SMH, upwelling is seen some 100 km directly upstream of the bump on the slope, and downwelling over the bump as flow is deflected anticyclonically into the deeper water. The temperature contours show that the deflection results in seaward advection of the near-surface shelf water on the outer shelf west-southwest of the bump and upwelling is induced to compensate. Upwelling is also seen along the shelfbreak and on the outer shelf in the cyclonic region downstream and shoreward of the bump. The downstream extension (from the position of maximum

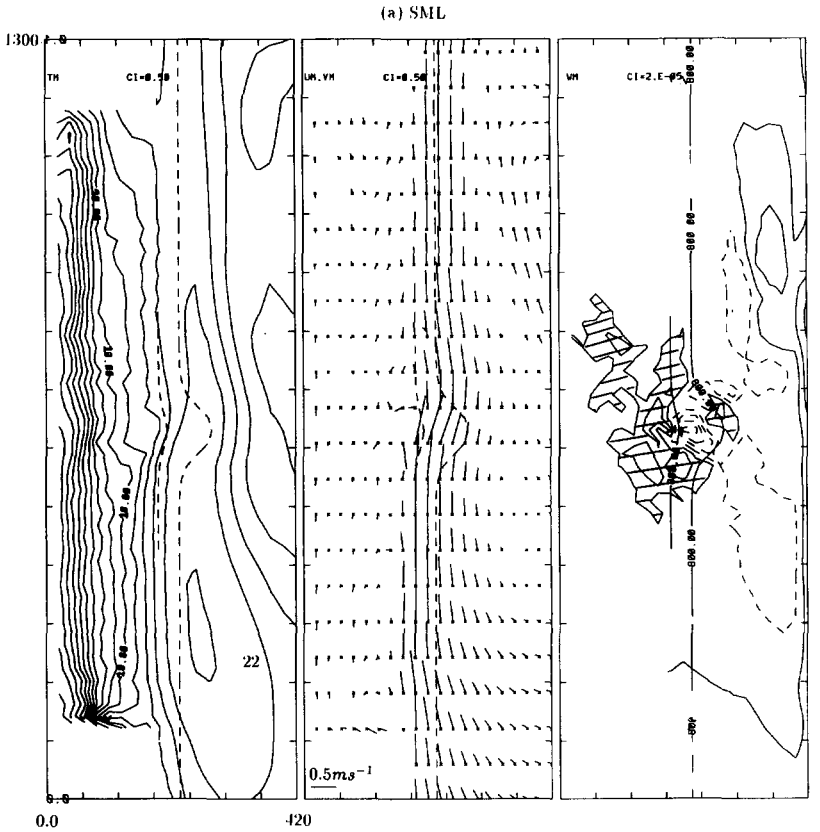


Fig. 4. The near-surface mean temperature contours (left panel), velocity vectors (middle panel) and vertical velocity contours (right panel; negative contours are dashed) for experiments (a) SML and (b) SMH, plotted in a blown-up region which includes the shelf as well as the WBC in the Bight. For the temperature and horizontal velocities, the first $\sigma$ grid level below the surface is used, while for the vertical velocity, a depth-averaged value over the upper three $\sigma$ levels are used. The vectors are plotted at each grid points in the cross-shore direction and at every three grid points in the along-shore direction. The 300 and 800 m isobaths are plotted to indicate the location of the bumps, and upwelling velocity magnitudes greater than $2 \times 10^{-5}$ m s$^{-1}$ in the vicinity of the bumps are hatched.

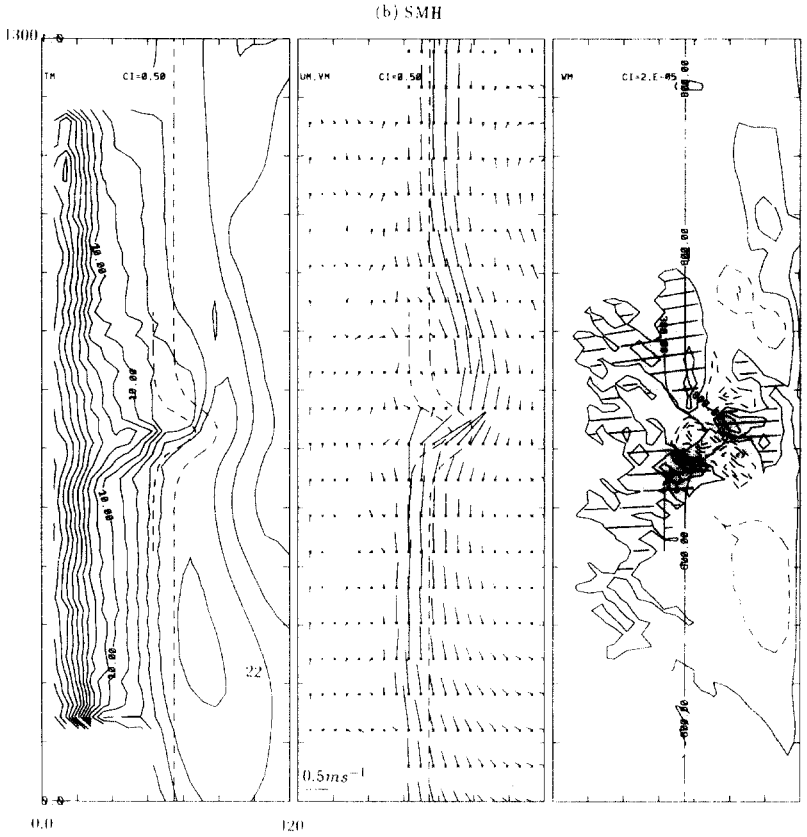


Fig. 4. (continued)

deflection of the bump) of this upwelling region is approximately 150 km for SML, and 300 km for SMH. These upwelling centers (where vertical velocity magnitudes are greater than $2 \times 10^{-5}$ m $s^{-1}$) are important physically, and are also important to ecological processes of the shelf and shelfbreak regions. Observations in the vicinity of the Charleston Bump often show cool water and high chlorophyll values indicative of upwelling along the shelfbreak (i.e. shoreward of the bump, Singer et al., 1983). The observed upwelling may be produced by the same flow kinematics as those which occur in the model results. Figure 4 also shows that the main axis of the WBC is displaced approximately 40 km (for SML) to 60 km (for SMH) seaward as parabathic flow downstream of the bump resumes. Such mean displacement, of magnitude of approximately 30–40 km measured from the 200 m isobath, has been observed for the Gulf Stream downstream of the Charleston Bump (Olson et al., 1983).

*Meander development*

The cyclonic region downstream of the bump (Fig. 4) can be interpreted as the cumulative effect of slope-bound cyclonic recirculations of meanders which develop following the deflection of the model WBC by the bump. We give here the results obtained with experiment SML which as noted earlier has a bump amplitude most similar to that of the Charleston Bump. The results for experiment SO are not presented, since it produces no finite-amplitude meanders which resemble the observed features (see OC). Figure 5 shows contours of temperature and velocity vectors at $z = 175$ m, for time (a) 3149, (b) 3161, (c) 3173 and (d) 3185 days. The subsurface is chosen in order to see more clearly the effect of the bump. In these plots, a meander denoted by "S" (for "stationary") exists immediately downstream of the maximum cross-shore amplitude of the bump (the $y$-position of which is

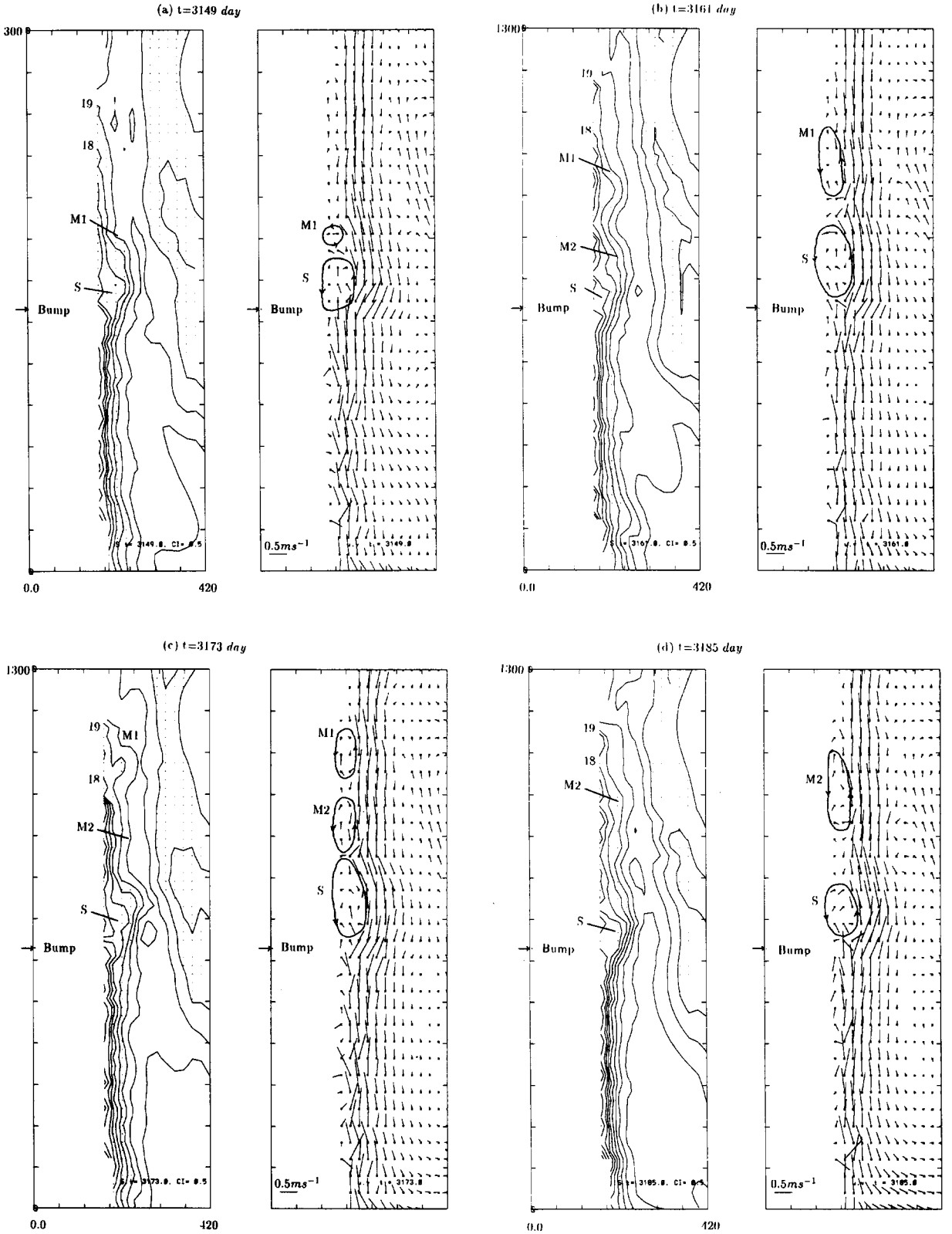


Fig. 5. Experiment SML: the temperature contours (left panel) and velocity vectors at $z = -175$ m, for times (a) 3149, (b) 3161, (c) 3173 and (d) 3185 days. The vectors are plotted at each grid point in the cross-shore direction and at every other grid point in the along-shore direction. Temperature contour interval is 1°C for $T < 19$°C, and 0.5°C for $T > 19$°C.

marked as "bump" in Fig. 5) and a cyclonic re-circulation is found shoreward of "S". The meander measures approximately 60–80 km from the 175 m isobath, the shoreward-most position for which no contours or vectors are shown in Fig. 5, and is clearly a result of the deflection of the WBC by the bump. If we define a deflection amplitude of less than or more than 60 km to be a "small" or "large" deflection, respectively we obtain from the 265 days analyzed, that approximately 28% of the time the WBC deflection at the bump is "large". The deflection generates disturbances downstream of the bump, as can be seen by following them with plots at more closely spaced time interval (not shown). Figure 5 shows examples for disturbances "M1" (Fig. 5a, b) and "M2" (Fig. 5b, c, d) which eventually mature into finite-amplitude meanders downstream of the bump with distinct cyclonic re-circulations on their shoreward sides (Fig. 5b, d). Thus, flow deflected at the bump does not appear to directly shed meanders downstream. Rather, these downstream meanders develop as a result of growths of small-scale cyclonic perturbations produced by the deflection. The amplification is perhaps due to a combination of baroclinic and barotropic instability processes, with the bump acting as the "trigger", as hypothesized in Oey (1988). The recent work by Mitsudera and Grimshaw (1991) using a two-layer quasi-geostrophic model also appears to support this viewpoint, but needs to be verified by more analyses of the results obtained from the present primitive-equation model. The above results show nevertheless that meanders downstream of the bump possess features which are similar to those observed in the vicinity of the Charleston Bump in the SAB, with approximately the correct alongstream and cross-stream scales of about 150–250 km and 30–60 km, respectively (see, e.g., Bane, 1983). However, the meander phase speeds of 0.1 to 0.3 m $s^{-1}$, estimated from Fig. 5, are too slow, probably because the stream in the model is too slow, about 0.5 m $s^{-1}$ at 175 m depth (Fig. 5).

In addition to downstream variability, perturbations also exist upstream of the bump in Fig. 5, wherein meander waves can be seen, albeit of smaller amplitudes than those develop downstream of the bump; this again is in accord with observations (Lee and Atkinson, 1983; Bane, 1983). At times we see relatively large onshore–offshore directed flows along the shelfbreak south of the bump (Fig. 5a, c). These indeed reflect correspondingly large perturbations near the surface, as shown for example for $t = 3149$ days in Fig. 6. Here, temperature contours and vectors at $z = -30$ m are plotted. Over the shelf, the vectors show large cross-shelf currents upstream of the bump, and weaker shelf currents north of the bump. We now present statistics to support these inferences from the synoptic results.

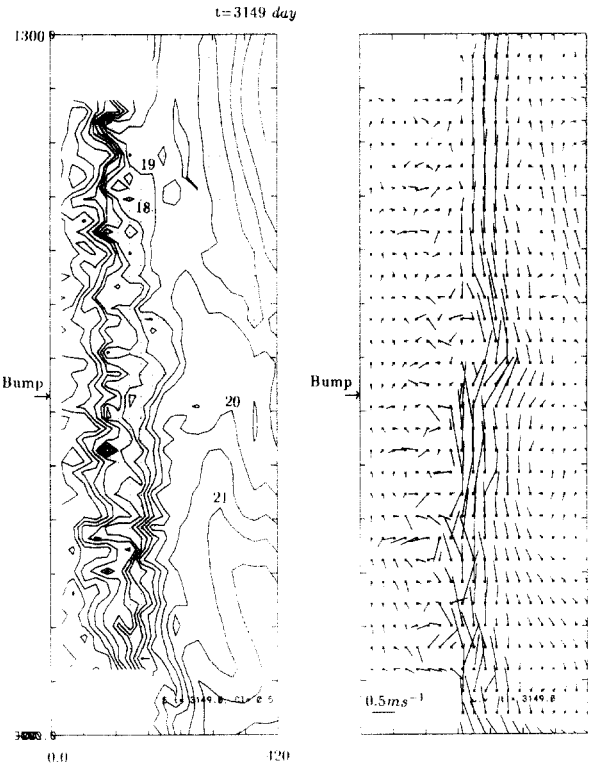

Fig. 6. Same as Fig. 5a at $z = -30$ m.

*Flow statistics*

Figure 7 compares contours of time-averaged perturbation kinetic energies of the depth-averaged horizontal velocities ($\langle u_a'^2 + v_a'^2 \rangle$, where the subscript "a" denotes depth averaging, the prime denotes perturbation and $\langle . \rangle$ denotes time averaging) and variances of the perturbation free-surface elevations for experiments (a) SO, (b)

SML and (c) SMH. Where no ambiguity exists, we will simply refer to these as the kinetic energy and elevation variance, respectively. The perturbation velocities and elevations are obtained by removing the corresponding 265-day mean values, and the mean elevations and depth-averaged velocity vectors are also shown in Fig. 7. A few important inferences can be made from these simple statistics. First, the net transports on the shelf (as inferred from the depth-averaged velocity vectors) are southward for all three experiments and are most intense for experiment SO. The southward velocity is trapped at the coast where the largest magnitude of about 0.15 m $s^{-1}$ is found, and the flow intensifies as it exists across-shelf into the open ocean along the southern coast of the Bight, most likely due to stretching of the water column as it enters the slope. The southward transport on the shelf is therefore balanced by a net inflow across the shelfbreak. This net across-shelfbreak inflow is consistent with the computed northward sea-level rise along the Bight (Fig. 7) but is in contrast with the results found in OC in which the model WBC is deflected by a bottom bump as well as by a coastal wall located in the northern Bight. In this latter case, mean sea-level decreases northward and the net transport is seaward across the major portion of the shelfbreak. The effect of the bump and coastal wall in that case is to produce a local sea-level low inshore of the bump. This effect can also be seen in Fig. 7 by comparing experiments SML and SMH with SO. Comparison of experiments SO and SMH further shows that the mean southward transport for the shelf portion south of the bump is weaker in the case of SMH, suggestive of an off-shore flow tendency induced by the bump. The same is also true when comparison is

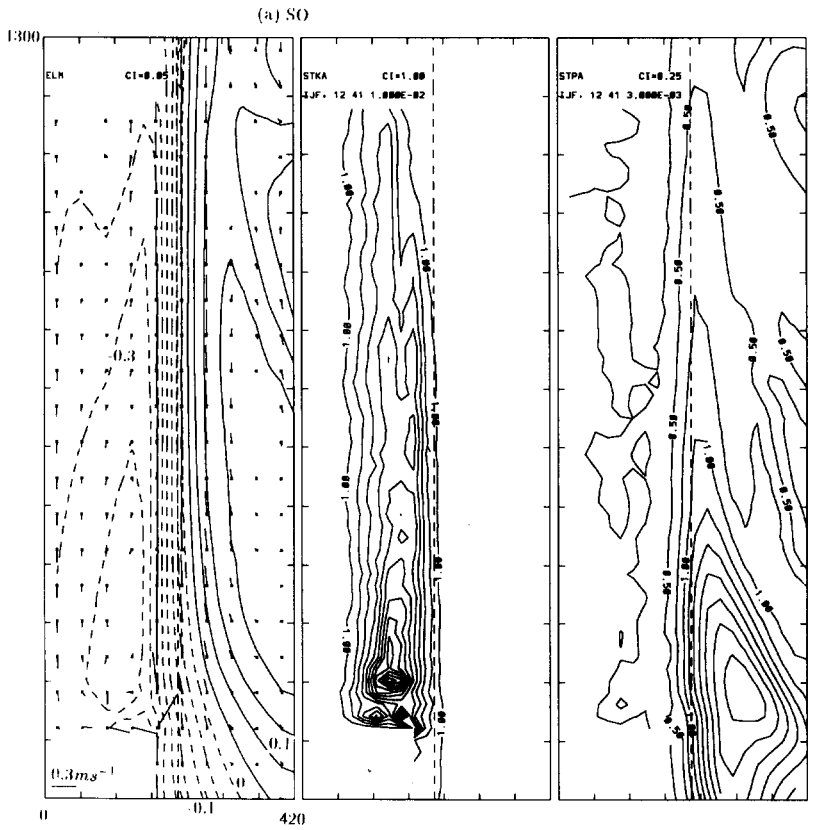


Fig. 7. The mean elevation contours and depth-averaged velocity vectors (left panel), the kinetic energy of the perturbation depth-averaged velocities (normalized by $10^{-2}$; middle panel), and the variance of the perturbation elevation (normalized by $3 \times 10^{-3}$; right panel) for experiments (a) SO, (b) SML and (c) SMH.

made between SO and SML, but the difference is less. We will later present results from the Gulf Stream simulation and elaborate further on the above inferences about the mean sea-level forcing in the SAB.

The time-dependent part of the flow which makes up the trapped coastal mean transport can be interpreted as consisting of a series of (under-resolved) coastally trapped waves which propagate cyclonically around the Bight and which eventually exit along the southern shoreline of the Bight. We have not been successful in identifying how these waves are generated: whether they are forced in the north by shoreward intrusions due to propagating meanders, or by deep ocean wave-like disturbances which are found to occasionally enter the Bight region from further south. It is likely that both processes are active. The kinetic energy plot for experiment SO (Fig. 7a, middle panel), as well as the elevation variance (right panel), show maxima in the south and a northward decrease, suggestive of a forcing derived from the wave-like disturbances from the south. Contour plots of the computed perturbation fields for the entire ocean basin (not shown) suggest that the disturbances are produced by Rossby wave-like propagation from the east along the westward-flowing drift of the "sub-tropical gyre", and are perhaps a result of dispersion and diffraction as these waves impinge upon the western boundary of the ocean. Note that the effect of the bump is to move the center of maximum variance southward, more so for SMH than for SML, a result which may be related to the dispersion and diffraction of waves. Lee and Atkinson (1983) also found a decrease in eddy kinetic energy northward from the Florida Strait along the inshore edge of the Gulf Stream, in agreement with the modeled decrease presented here. The source of the energy is not known, however.

A comparison of the kinetic energy and elevation variance (Fig. 7, right panels) for SO, SML

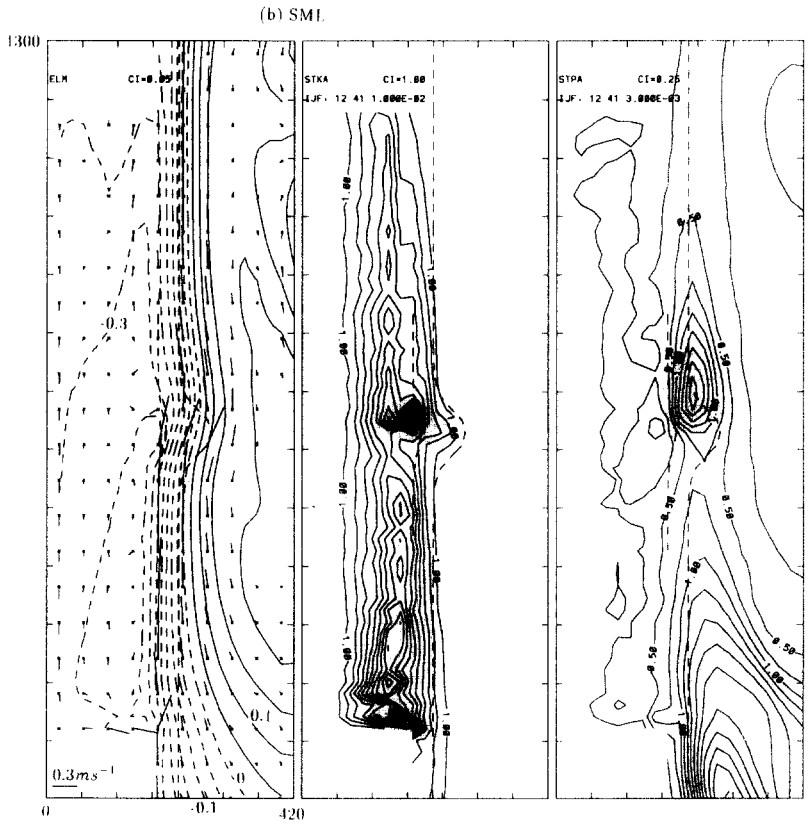


Fig. 7. (continued)

and SMH shows that the effect of the bump is to increase the flow variabilities on the shelf both upstream and downstream of the bump, especially in term of the flow's kinetic energy. The increase downstream is readily understood in term of meanders which develop there as a result of flow deflection at the bump, as discussed above. The increase upstream is interpreted as being caused by upstream topographic wave propagation, and the wave source is over the bump where meanders of the WBC are produced. As in OC, the wave is embedded in the northward current, and a stationary wavelength is estimated for the present model's slope and current strength to be about 100–150 km (Pedlosky, 1979). The kinetic energy plots for SML and SMH (Fig. 7b, c) show regions of local maxima on the outer shelf and shelfbreak at multiples of 100–150 km upstream of the bump. The increases over the kinetic energy for SO are about 30 to 40%, and are therefore significant. OC interpreted such local maxima as being caused by enhanced diabathic (cross isobath) motion as a result of interaction between the stationary topographic wave and frontal meander. Figure 7 also shows that, although elevation variance generally increases shoreward of the bumps, the variance for SML is actually larger than that for SMH. Note that, in all experiments, the root mean squared value of the elevation is approximately 3 cm on the shelf, and reaches a maximum of about 8 cm downstream of the bump for SML. Coastal sea-level perturbations from the WBC is therefore quite significant.

Figure 8 compares the near-surface contours of perturbation kinetic energies, $\langle u'^2 + v'^2 + w'^2 \rangle$ (middle panels), and variances of the perturbation temperature (right panels) for experiments (a) SO, (b) SML and (c) SMH. For ease of comparison, the mean near-surface temperature and velocity vectors are also given (left panels). The plots show increased variabilities upstream as well as downstream of the bump. The temper-

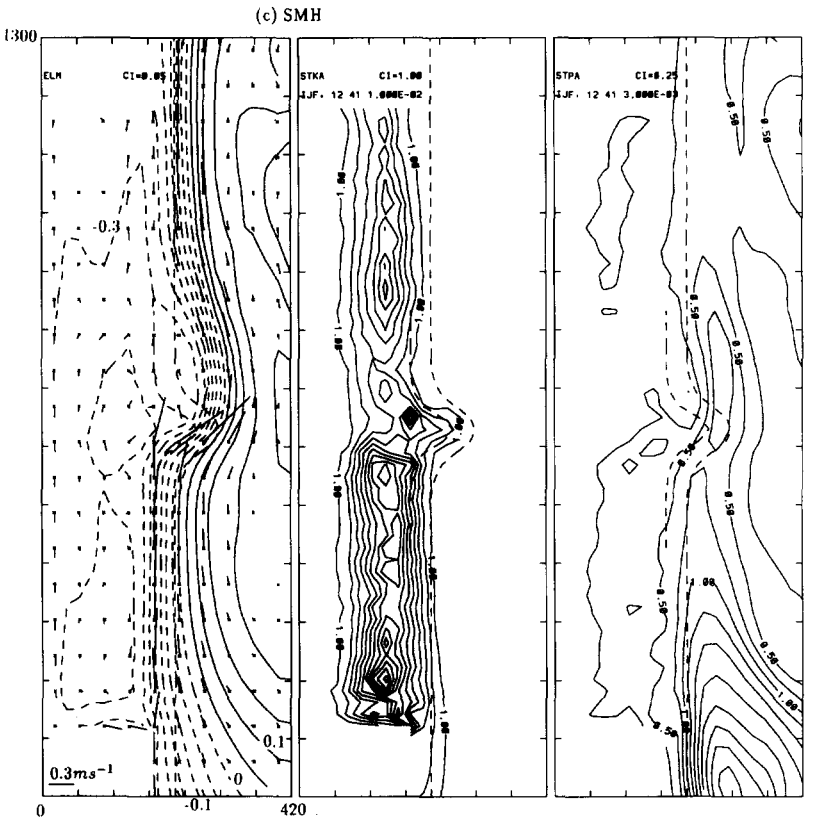


Fig. 7. (continued)

ature variance shows a root mean squared increase of about 1°C and the velocity about 0.2 m $s^{-1}$ over the shelf from experiment SO to SML and SMH, due apparently to increased cross-shelf exchange of water mass in the presence of the bumps. A substantial portion of the kinetic energy increase is due to $\langle u'^2 \rangle$ (approximately 60%; plots not shown), and this occurs over the sloping region of the shelf just inshore of the 200 m isobath on the outer shelf and shelfbreak. Upstream of the bump, the increase is therefore likely to be caused by trapped topographic wave activity on the outer shelf and shelfbreak. Downstream of the bump, the increase is due to perturbations caused by propagating meanders produced by the bump as described previously, and it extends some 100 km further north for SMH than for SML. While we plot in Fig. 5 fields at $z = -175$ m, corresponding meanders are also present near the surface, except that the features are more complex (see, e.g. Fig. 6) in part because of the imposed surface cooling. The near-surface meanders produce episodic shoreward intrusions which appear to be confined within narrow cross-shelf "jets", as the temperature contours and vectors in Fig. 6 also show. However, the jets may not be well resolved by the 20 km grid sizes used in the model. The intrusions bring warm water onto the shelf, and this couples with the imposed atmospheric cooling to produce a strong temperature variance along the mid-shelf (Fig. 8b, c). The response near coast is perhaps in the form of trapped baroclinic Kelvin waves.

To see if the increased flow variabilities upstream of the bump are related to perturbations produced over the bump, we have computed the spatial autocorrelation of the perturbation temperature and elevation with zero lag at the lati-

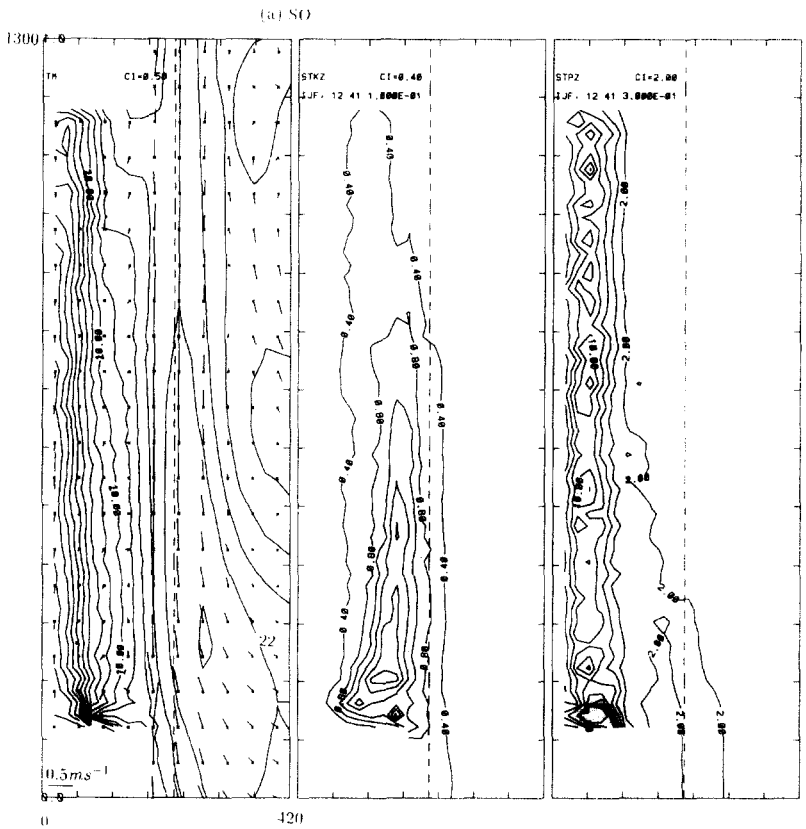


Fig. 8. The near-surface (at first $\sigma$ grid level) mean temperature contours and velocity vectors (left panel), the kinetic energy of the near-surface perturbation velocities (normalized by $10^{-1}$; middle panel), and the variance of the near-surface perturbation temperature (normalized by $3 \times 10^{-1}$; right panel) for experiments (a) SO, (b) SML and (c) SMH.

tude of the bump's maximum deflection just inshore of the 800 m isobath (or, in the case of experiment SO, at the same latitude and also inshore of the 800 m isobath). These are plotted as the left and middle panels, respectively, in Fig. 9 for experiments (a) SO, (b) SML and (c) SMH. In SO, auto-correlation of the elevation is skewed about its maximum of "1" in the downstream direction for values greater than "0.7", the 95% confidence level. The auto-correlation of the temperature is less skewed, but the downstream asymmetry is still evident. In contrast, the plots for SML and SMH are skewed about the maximum in the upstream direction for values greater than "0.7" (although the "0.6" contour is more symmetrical). The skewed contours also appear to follow the isobath especially in the case of elevation. The analysis thus shows significant upstream influence when the bump is present, and supports the idea that topographic waves are responsible in generating flow variabilities upstream of the bump, as suggested previously in connection with the eddy kinetic energy plots in Figs. 7 and 8.

Figure 9 (right panels) also compares the cross-correlation of the perturbation cross-shore velocity $u'$ and temperature $T'$ (non-dimensionalized by the product of the root mean squared values of $u'$ and $T'$), for the near-surface grid point. A negative $\langle u'T' \rangle$, coupled with positive cross-shore mean temperature gradient indicates baroclinic instability with growing perturbation potential energy. For SO, the region inshore of the model WBC is baroclinically unstable. The plot for SML is similar. For SMH, the region just upstream of the bump is baroclinically stable ($\langle u'T' \rangle$ is positive), while larger (relative to those of SO and SML) negative values are found downstream, indicating enhanced baroclinic instability. In Fig. 10, we also compare the cross-correlation of the perturbation cross-shore velocity $u'$ and along-shore velocity $v'$ (non-dimensionalized by

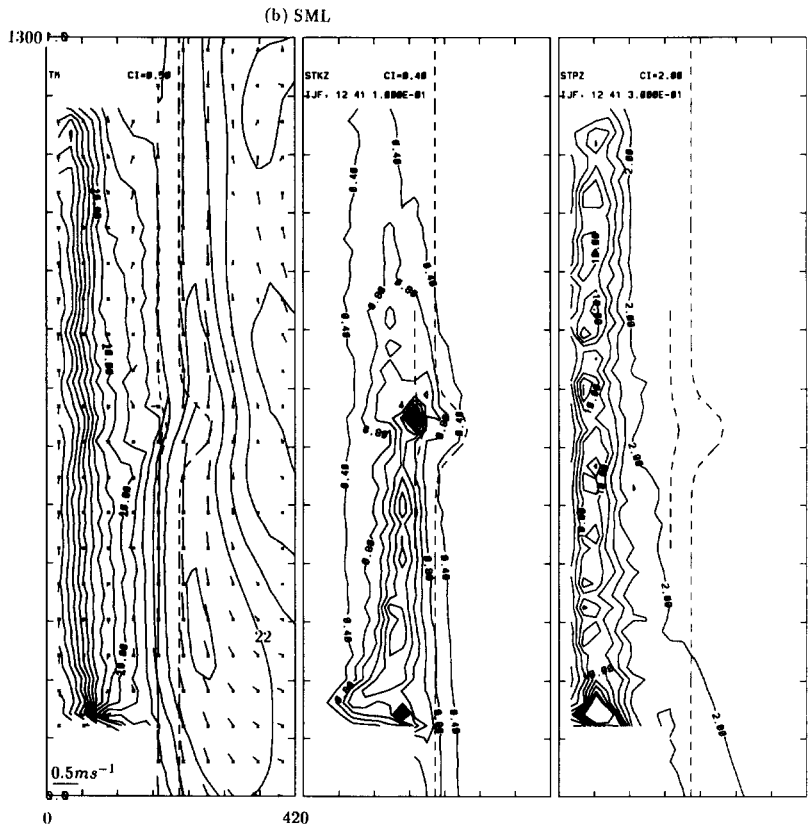


Fig. 8. (continued)

the product of the root mean squared values of $u'$ and $v'$), for the near-surface grid point. A negative $\langle u'v' \rangle$, coupled with positive cross-shore mean (along-shore) velocity gradient, which is generally true inshore of the model WBC, would indicate barotropic instability with growing perturbation kinetic energy. For SO (Fig. 10, left panel), the flow appears to be barotropically stable. For SML (middle panel), there is a small region of barotropic instability just inshore of the bump where $\langle u'v' \rangle$ is negative. For SMH (right panel), there is an additional region of instability downstream of the bump; this region coincides fairly well with the region of baroclinic instability as was indicated in Fig. 9c. These results support the view mentioned earlier in discussing meander development downstream of the bump (Fig. 5) that disturbances generated over the bump are amplified downstream by dynamic instability.

## The Gulf Stream model

The above results from a model with idealized bathymetry of increasing complexity (shelfbreak with parallel isobaths, shelfbreak with bump, and shelfbreak with bump plus blocking in OC) have provided insights into the dynamics and thermodynamics of a WBC and its meanders along the continental slope. To further our understanding we now present results from a simulation of the Gulf Stream in the SAB, forced by realistic lateral transport, temperature and salinity, as well as by monthly winds and heat fluxes. The objectives will be to examine if the inferences derived from the simpler models with regard to flow variabilities generated by a bump can be verified, and if the effect of the Charleston Bump can be interpreted in terms of the component dynamics of the models with simple bathymetry.

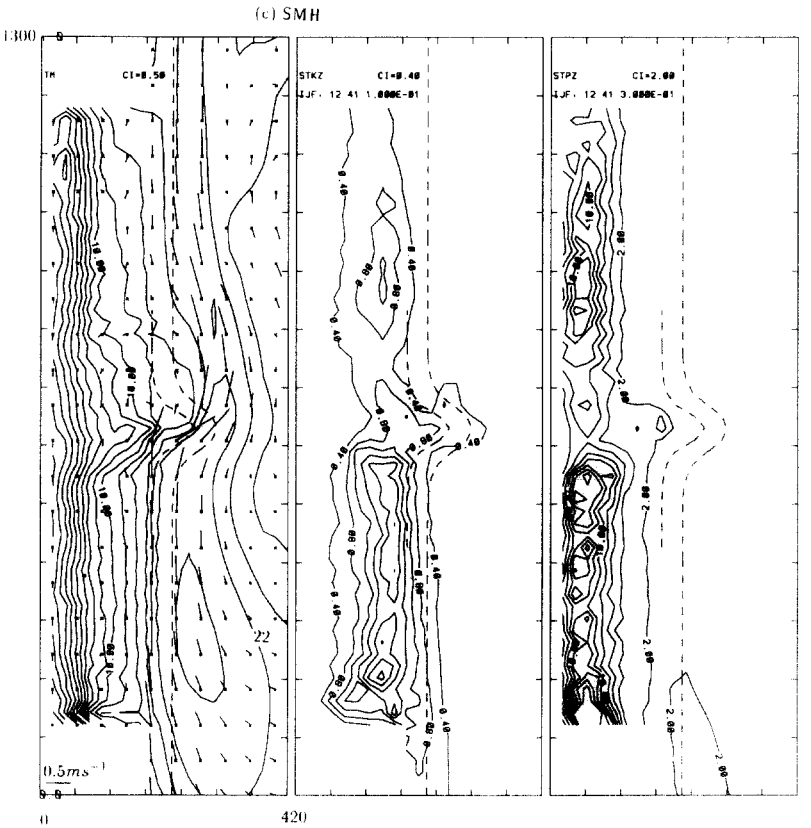


Fig. 8. (continued)

The simulation employs the same governing equations and numerical scheme as those used in the simpler models. Details of the model formulation are described in Mellor and Ezer (1991). The model domain actually extends from the Florida Straits to the region just west of the New England Seamount chain, but for the present application we examine the results in the SAB only. The boundary forcings are improved over those used in Mellor and Ezer (1991), in that instead of the annual means, we now used monthly winds and heat fluxes at the surface, and seasonal salinity and temperature fields at the southern boundary across the Florida Straits (details are described by Ezer and Mellor, 1991). In the SAB portion of the model, an inflow transport of 30 Sv across the Straits and 30 Sv across the eastern open boundary are specified. Figure 11 shows the bathymetry and model grid in the SAB, in which one sees the (somewhat smoothed) Charleston Bump at about the 31.5°N. The cross-shelf grid sizes are small, approximately 5 km, in the shelfbreak and slope where the main axis of the Gulf Stream is expected, and expand shoreward and seaward with a maximum of about 20 km near the eastern open boundary. The along-shelf grid is more uniform (from 10 to 20 km). Note that the model's coast is defined at the 20 m isobath. Model simulation was carried out for 5 years initialized from a diagnostic calculation in which the velocity field was in equilibrium with the density field specified from observation (for details see Mellor and Ezer, 1991). It is the final year's results which we will analyze and discuss below. No attempt is made to specifically analyze the winter results, since the conclusions

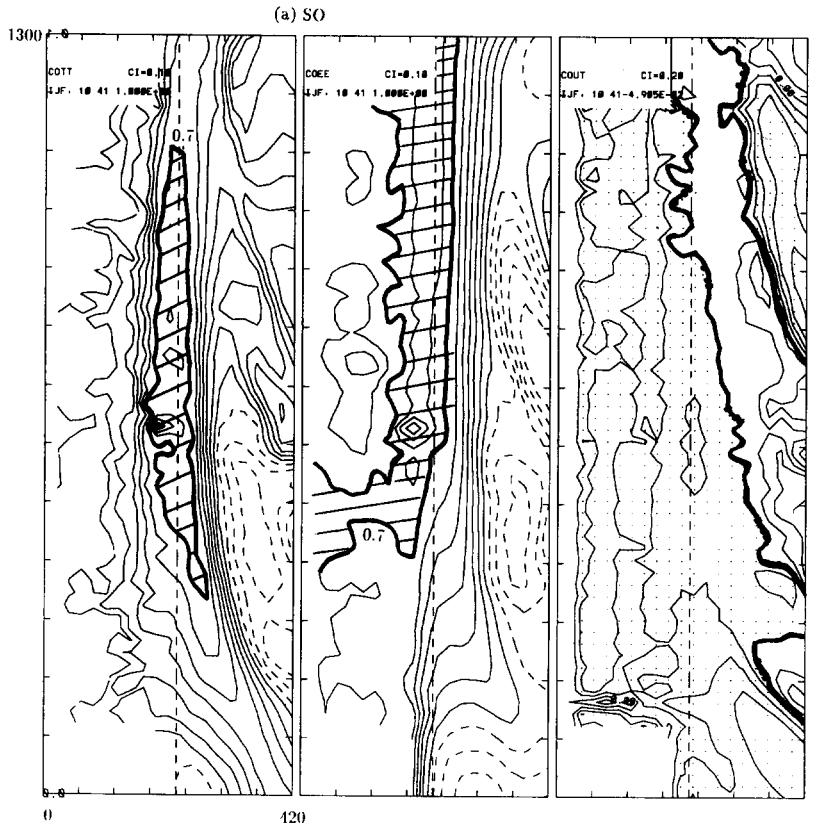


Fig. 9. The spatial auto-correlations of the near-surface, perturbation temperature (left panel) and elevation (middle panel), and the cross-correlation between perturbation cross-shore velocity $u$ and temperature $T$ (right panel; thickened contour = 0 and negative regions are stippled) for experiments (a) SO, (b) SML and (c) SMH. For the auto-correlation plots, negative contours are dashed, thickened contour = 0.7 and regions greater than 0.7 are hatched.

derived from the simpler model (designed to mimic a wintertime cooled shelf) in regard to meander development and energetics should be valid, approximately, for all seasons.

*Meander development*

Examination of the simulated temperature fields show that the Gulf Stream's path over the Charleston Bump exists in two states: a small or no meander state (henceforth SMS) and a large meander state (henceforth LMS). These two states are analogous to the small and large deflection states found in the previous section for the simpler model. Whether the different states are caused by the seasonal boundary forcing, or by internal flow dynamics are not clear although the large meander state is found to occur most often from autumn through early winter (September through January), approximately 31% of the time for one year's simulation. Figure 12 shows the simulated temperature contours, at $z = -30$ m from August 5 through September 10 at 5 days interval, which illustrates instances when the SMS (August 5) transists (August 10 through 30) into the LMS (September 5 and 10; see in particular the meander denoted as "M2" in the figure). The Gulf Stream path at the SMS lies inshore of the Bump along approximately the 300 m isobath, while that at the LMS is deflected further offshore by the Bump, so that approximately half of the Stream lies over the deeper water regions where water depths are greater than 600 m. In this latter case, the solution displays the type of "current branching" described in Oey (1988). In Oey's work, the SMS an LMS are two possible solutions which result from amplification of baroclinically unstable waves, and are likely to be functions of upstream parameters: depth of the main thermocline and transport, for examples. More analyses, coupled perhaps with more process-oriented SAB simulations with simpler forc-

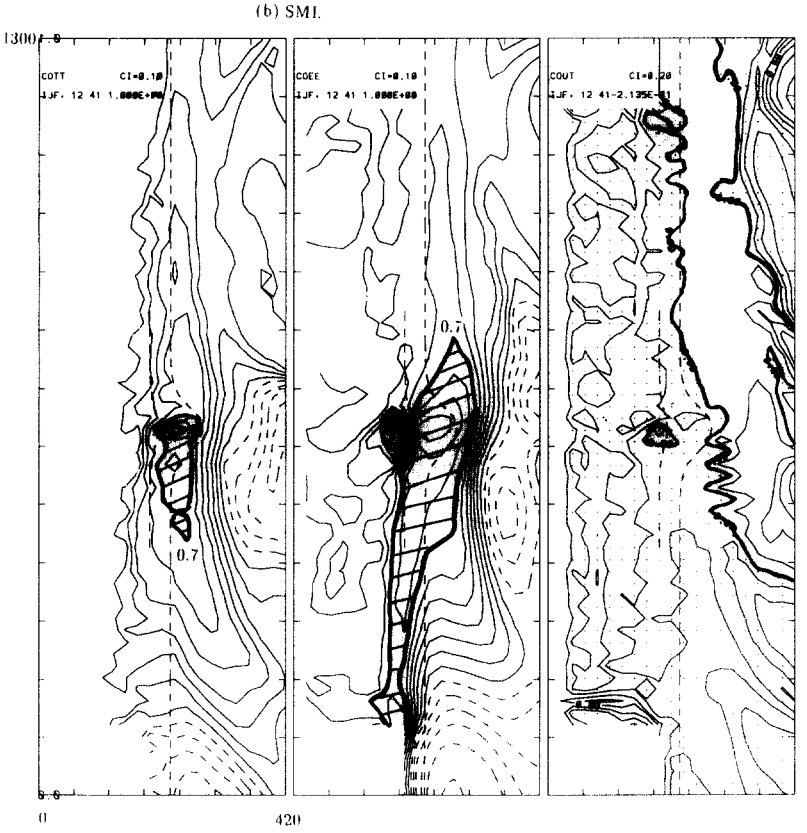


Fig. 9. (continued)

ing, are clearly needed to further clarify the flow dynamics. At present, it suffices to note that the simulation has produced many of the realistic features of the Stream and its meanders. In particular, the two meanders downstream of the Charleston Bump on August 30 are strikingly similar to those observed by Bane (1983), with an along-stream scale of about 150–200 km and a cross-stream scale of about 30–50 km.

*Flow statistics*

Figure 13 gives the mean surface elevation (left panel) and the root mean squared perturbation elevation (right panel). The mean elevation shows a low just downstream of the bump, similar to that found in Fig. 7b, c for experiments SML and SMH. Along the entire Bight, the elevation decreases. This is in part caused by the Charleston Bump, but is primarily attributed to the bending of the SAB from a south/north direction south of the 32°N to a southwest/northeast direction further north, as can be inferred from OC in which a WBC deflected by a coastal protrusion was simulated. The rms elevation shows a high just downstream of the Bump, in agreement with Fig. 7b for experiment SML, and the southwestward extension of the contours, as well as those seen on the outer shelf south of the bump (weak signals can also be seen for experiments SML and SMH, cf. Fig. 7b, c with a) show the upstream influence of the bump. Figure 14 gives the perturbation kinetic energy ($\langle[u'^2 + v'^2]/2\rangle$ in $cm^2\ s^{-2}$) at $z = -30$ m. Both the rms elevation and perturbation kinetic energy show larger values in comparison with those of experiments SML and SMH, caused by the larger transport specified in the realistic simulation, and perhaps also by the variable forcing. The perturbation kinetic energy shows a local maximum inshore and just downstream of the bump (cf. Figs. 7b and 8b), as well as a maximum over the seaward

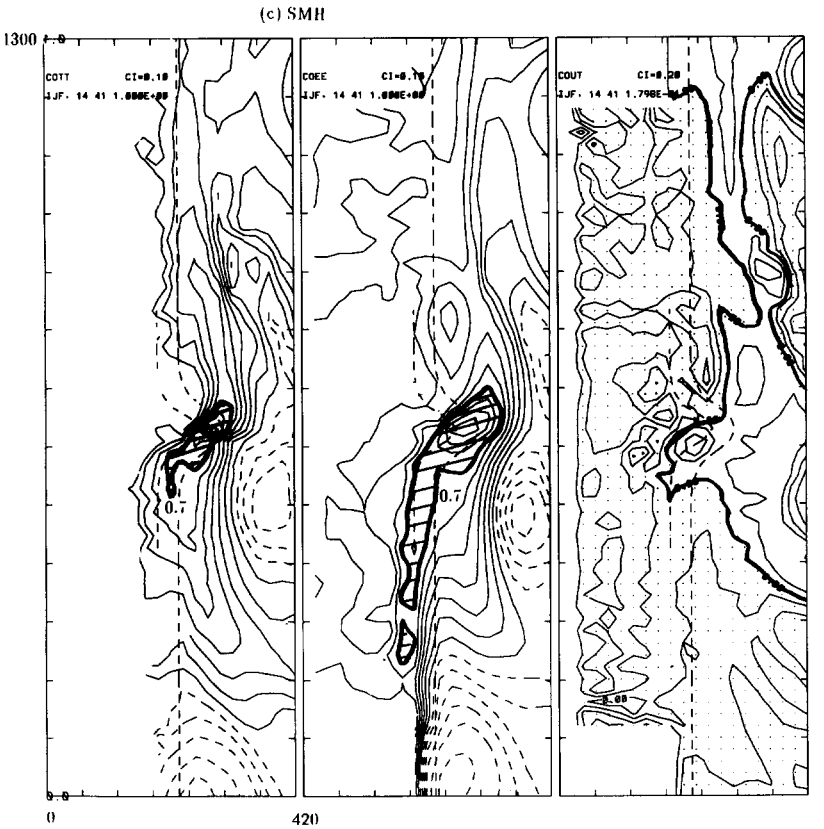


Fig. 9. (continued)

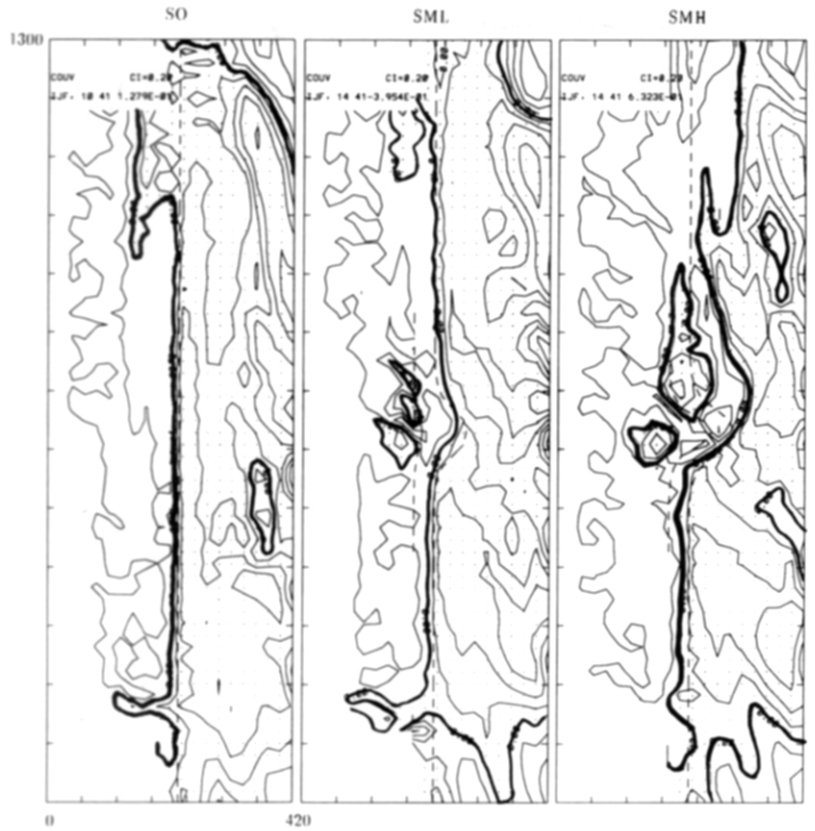


Fig. 10. The cross-correlation between perturbation cross-shore velocity $u$ and along-shore velocity $v$ for experiments SO (left panel), SML (middle panel) and SMH (right panel). Thickened contour = 0 and negative regions are stippled.

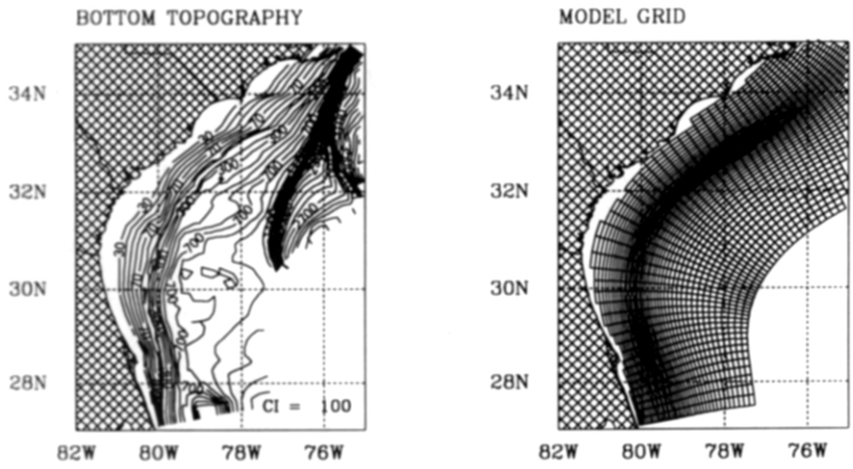


Fig. 11. The topography (left panel) and grid (right panel) used for the Gulf Stream simulation in the SAB. The contour interval for the topography is 10 m on the shelf and 100 m offshore.

edge of the bump. This seaward maximum is not seen in Figs. 7b and 8b for experiment SML, perhaps because the "bump" size used (with an offshore deflection of about 60 km) is smaller than that for the Charleston Bump, which has an offshore deflection of about 150 km. The offshore maximum in the realistic simulation case is clearly due to the large meander state of the Gulf Stream path as discussed above. The variability is intense downstream of the bump as expected since energetic meanders are often formed (cf. Figs. 7 and 8), but the plot also shows a local maximum on the shelfbreak/outer shelf some 150–200 km upstream of the bump. We see no obvious reason why a local energetic variability in the Stream should occur there. The Stream hugs close to the shelfbreak in waters of 500 m depth or less in this region and a local seaward deflection of the 800 m isobath (Fig. 11) south of 30°N does not appear to have any effect on the model Stream path. On the other hand, the upstream distance of this local maximum coincides well with the first node of a stationary topographic wave generated by the interaction of the Stream with the Charleston Bump, and as shown in OC, this can give rise to locally intense current variability. The same upstream variability was noted earlier for experiments SML and SMH (Figs. 7b, c and 8b, c), although there are several maxima. Finally, we show in Fig. 15 the spatial auto-correlation of the perturbation (a) elevation and (b) temperature at $z = -30$ m, with zero lag over the Charleston Bump. The contour for correlation values greater than "0.7" extends both downstream and up-

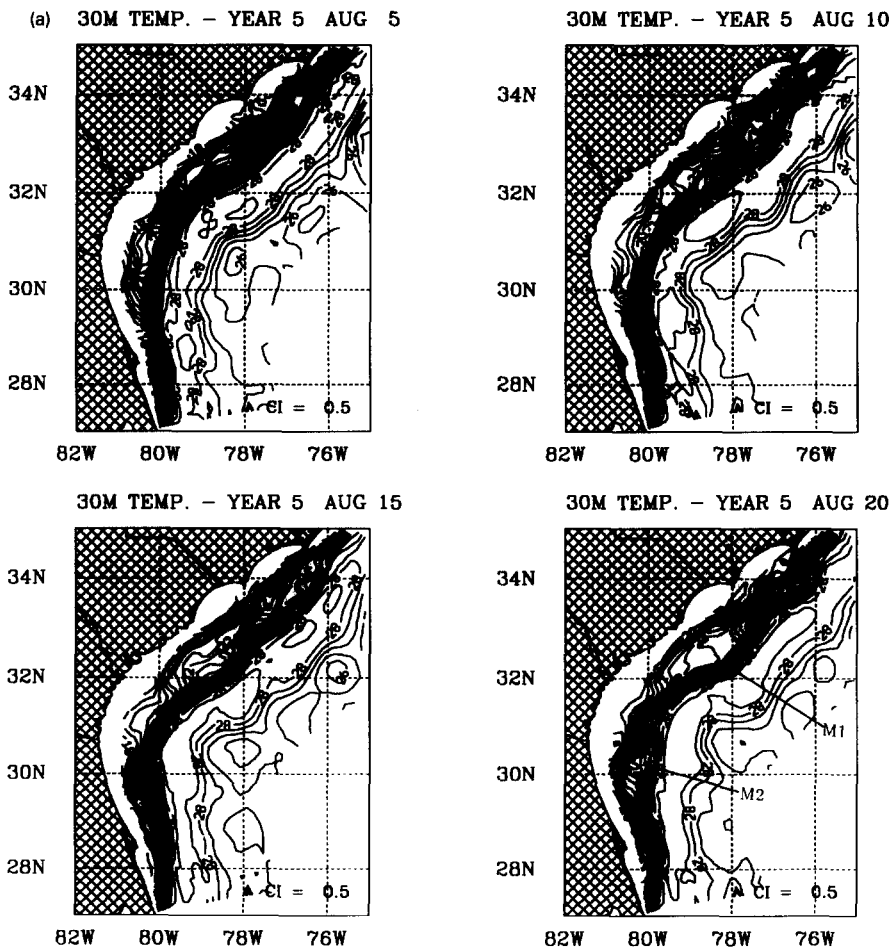


Fig. 12. The simulated Gulf Stream temperature at $z = -30$ m from August 5 through September 10 at 5 days' interval. The contour interval is 0.5°C.

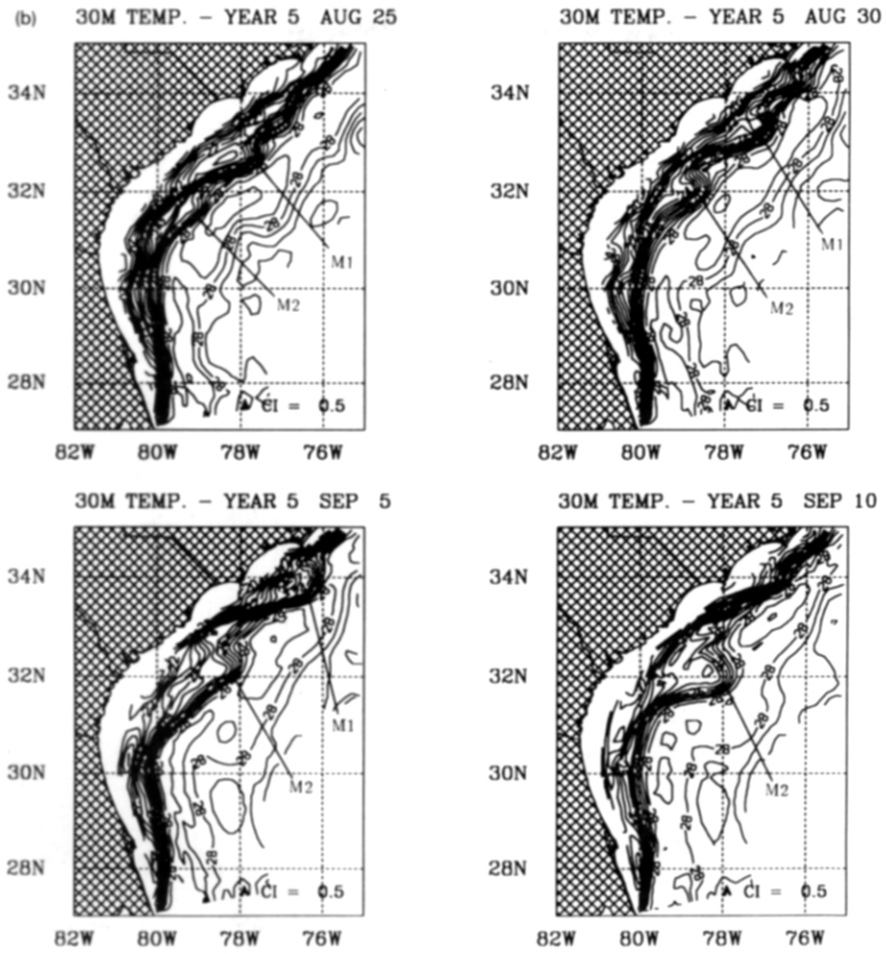


Fig. 12. (continued)

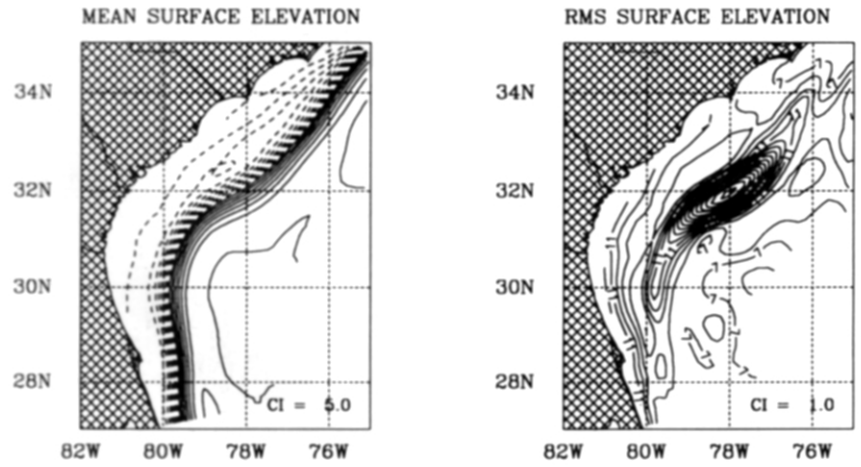


Fig. 13. The simulated Gulf Stream mean elevation (left panel) and root mean squared elevation (right panel) in the SAB.

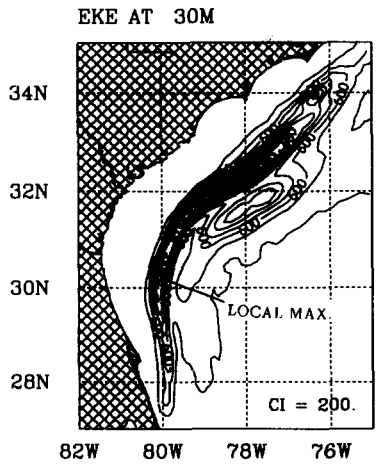


Fig. 14. The simulated eddy kinetic energy ($\langle [u'^2 + v'^2]/2 \rangle$ in $cm^2\ s^{-2}$) at $z = -30$ m in the SAB.

stream of the bump, approximately following the slope. The upstream extension, together with Fig. 14, further indicates significant upstream influence, and this may in part be caused by propagation of topographic wave produced by energetic meanders over the bump.

## Conclusion

An important objective of the present study is to examine if finite-amplitude WBC meanders can be realized even in the presence of the stabilizing influence of a continental slope. This problem is considered herein with numerical experiments of a WBC perturbed by a topographic bump. We find that energetic current variabilities due to meanders are generated both downstream and upstream of the bump. Downstream variability is expected, but our results suggest that this is not merely a result of "eddy shedding" by flow interaction with the bump, but rather by meander amplification by flow instability. Upstream variability is clearly evident from comparing experiments with and without bumps, and we suggest that this is caused by upstream topographic wave propagation. Simulation results from a more realistic Gulf Stream model in the SAB lend support to the above findings. In the presence of bump, the modeled meanders (cross and along-frontal scales) are in good agreement with observations.

The identification of WBC variability upstream of a bump suggests upstream sources of frontal instability quite independent of wind, transport and other forcings, and may be important to the understanding of meander development further downstream. In the SAB, our simulation suggests an energetic source located on the shelfbreak some 200 km upstream of the Charleston Bump. It would be of interest to further pursue this by more extensive analysis of the simulation results, as well as perhaps to attempt to identify the source from observations.

In addition to meander development, the numerical experiments also indicate significant shelf variabilities as a result of the bump. These variabilities (in current as well as temperature) are important to the sub-tidal shelf dynamics, as well

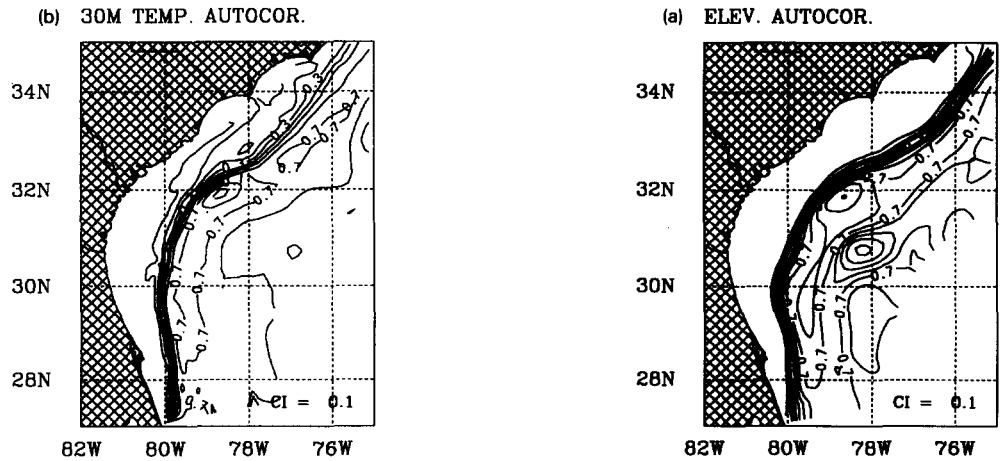


Fig. 15. The spatial auto-correlation of the perturbation (a) elevation and (b) temperature at $z = -30$ m in the SAB.

as to the ecosystem dynamics. A more detailed analysis of the simulation results on the effects of the Gulf Stream on the SAB shelf is needed to more realistically quantify the response.

## Acknowledgments

The support by the National Science Foundation under grant no. OCE-8711614 (LYO and PC), and by the Institute for Naval Oceanography, under contract no. INO-S8751 (LYO, TE and GLM), are gratefully acknowledged. Computer support was provided by the National Center for Supercomputing Applications, Illinois, the Pittsburgh Supercomputer Center and the Geophysical Fluid Dynamics Laboratory of NOAA, Princeton.

## References

Bane, J.M., Jr., 1983. Initial observations of the subsurface structure and short-term variability of the seaward deflection of the Gulf Stream off Charleston, South Carolina. J. Geophys. Res., 88: 4673–4684.

Blumberg, A.F. and Mellor, G.L., 1983. Diagnostic and prognostic numerical circulation studies of the South Atlantic Bight. J. Geophys. Res., 88: 4579–4592.

Chao, S.-Y. and Kao, T.W., 1987. Frontal instabilities of baroclinic ocean currents with applications to the Gulf Stream. J. Phys. Oceanogr., 17: 792–807.

Csanady, G.T., 1986: Radiation of topographic waves from Gulf Stream meanders. Cont. Shelf Res., 8: 673–686.

Ezer, T. and Mellor, G.L., 1992. A numerical study of the variability and the separation of the Gulf Stream induced by surface atmospheric forcing and lateral boundary flows. J. Phys. Oceanogr., 22: 660–682.

Hogg, N., 1981, Topographic waves along 70°W on the continental rise. J. Mar. Res., 39: 627–649.

James, I.D., 1987. A general three-dimensional eddy-resolving model for stratified seas. In: C.J. Nihoul and B.M. Jamart (Editor), Three-Dimensional Models of Marine and Estuarine Dynamics. Elsevier Oceanogr. Ser., 45. Elsevier, New York, pp. 591–608.

Lee, T.N. and Atkinson, L.P., 1983. Low-frequency current and temperature variability from Gulf Stream frontal eddies and atmospheric forcing along the southeast U.S. outer continental shelf. J. Geophys. Res., 88: 4541–4567.

Mellor, G.L. and Yamada, T., 1982. Development of a turbulence closure model for geophysical fluid problems. Rev. Geophys. Space Phys., 20: 851–875.

Mellor, G.L. and Ezer, T., 1991. A Gulf Stream model and an altimetry assimilation scheme. J. Geophys. Res., 96: 8779–8795.

Mitsudera, H. and Grimshaw, R., 1991. Generation of mesoscale variability by resonant interaction between a baroclinic current and localized topography. J. Phys. Oceangr., 21: 737–765.

Oey, L.-Y., Mellor, G.L. and Hires, R.I., 1985. A three dimensional simulation of the Hudson-Raritan estuary. Part I: Description of the model and model simulations. J. Phys. Oceangr., 15: 1676–1692.

Oey, L.-Y., 1988. A model of Gulf Stream frontal instabilities, meanders and eddies along the continental slope. J. Phys. Oceangr., 18: 211–229.

Oey, L.-Y. and Chen, P., 1991. Frontal waves upstream of a diabathic blocking: a model study. J. Phys. Oceangr., 21: 1643–1663.

Olson, D., Brown, O.B. and Emmerson, S.R., 1983. Gulf Stream frontal statistics from Florida Straits to Cape Hatteras derived from satellite and historical data. J. Geophys. Res., 88: 4569–4578.

Orlanski, I. and Cox, M.D., 1973. Baroclinic instability in ocean currents. Geophys. Fluid Dyn., 4: 297–332.

Pedlosky, J., 1979. Geophysical Fluid Dynamics. Springer-Verlag, 624 pp.

Singer, J.J., Atkinson, L.P., Blanton, J.O. and Yoder, J.A., 1983. Cape Romain and the Charleston Bump: historical and recent hydrographic observations. J. Geophys. Res., 88: 4569–4578.

Thompson, R., 1977. Observations of Rossby waves near site D. Prog. Oceanogr., 7: 1–28.

Wood, R.A., 1988. Unstable waves on oceanic fronts: large amplitude behavior and mean flow generation. J. Phys. Oceangr., 18: 775–787.

Xue, H., 1991. Numerical studies of Gulf Stream meanders in the South Atlantic Bight. Thesis, Princeton University, 188 pp.